

ARTICLE OPEN



Storage of photonic time-bin qubits for up to 20 ms in a rare-earth doped crystal

Antonio Ortu¹, Adrian Holzäpfel¹, Jean Etesse² and Mikael Afzelius¹✉

Long-duration quantum memories for photonic qubits are essential components for achieving long-distance quantum networks and repeaters. The mapping of optical states onto coherent spin-waves in rare earth ensembles is a particularly promising approach to quantum storage. However, it remains challenging to achieve long-duration storage at the quantum level due to read-out noise caused by the required spin-wave manipulation. In this work, we apply dynamical decoupling techniques and a small magnetic field to achieve the storage of six temporal modes for 20, 50, and 100 ms in a $^{151}\text{Eu}^{3+}:\text{Y}_2\text{SiO}_5$ crystal, based on an atomic frequency comb memory, where each temporal mode contains around one photon on average. The quantum coherence of the memory is verified by storing two time-bin qubits for 20 ms, with an average memory output fidelity of $F = (85 \pm 2)\%$ for an average number of photons per qubit of $\mu_{\text{in}} = 0.92 \pm 0.04$. The qubit analysis is done at the read-out of the memory, using a type of composite adiabatic read-out pulse we developed.

npj Quantum Information (2022)8:29; <https://doi.org/10.1038/s41534-022-00541-3>

INTRODUCTION

The realization of quantum repeaters^{1–3}, and more generally quantum networks, is a long-standing goal in quantum communication. It will enable long-range quantum entanglement distribution, long-distance quantum key distribution, distributed quantum computation, and quantum simulation⁴. Many schemes of quantum repeaters rely on the heralding of entanglement between quantum nodes in elementary links^{2,5}, followed by local swapping gates¹ to extend the entanglement. The introduction of atomic ensembles as repeater nodes, and the use of linear optics for the entanglement swapping, stems from the seminal DLCZ proposal². A key advantage of atomic ensembles is their ability to store qubits in many modes through multiplexing^{6–12}, which is crucial for distributing entanglement efficiently and with practical rates¹³.

Rare-earth-ion (RE) doped crystals provide a solid-state approach for ensemble-based quantum nodes. RE doped crystals can provide multiplexing in different degrees of freedom^{8,9,11,14–16}, efficient storage^{17,18}, long optical coherence times^{19,20}, and long coherence times of hyperfine states^{21–24} that allows long-duration and on-demand storage of optical quantum states. Long optical coherence times, in combination with the inhomogeneous broadening, offer the ability to store many temporal modes^{7,13}. Repeater schemes based on both time and spectral multiplexing schemes have been proposed^{8,13}. Here we focus on repeaters employing time-multiplexing and on-demand read-out in time¹³, which require the long storage times provided by hyperfine states²⁵.

The longest reported spin storage time of optical states with mean photon number of around 1 in RE doped solids is about 1 ms in $^{151}\text{Eu}^{3+}:\text{Y}_2\text{SiO}_5$ ²⁶. However, even near-term quantum repeaters spanning distances of 100 km or above would certainly require storage times of at least 10 ms, and more likely of hundreds of ms²⁵. A particular challenge of long duration quantum storage in RE systems is noise introduced by the application of the dynamical decoupling (DD) sequences that are required to overcome the inhomogeneous spin dephasing²⁶ and

the spectral diffusion^{22,24}. To reduce the noise one can apply error-compensating DD sequences²⁷, or increase the spin coherence time by applying magnetic fields to reduce the required number of pulses^{22,28,29}.

In this article we report on an atomic frequency comb (AFC) spin-wave memory in $^{151}\text{Eu}^{3+}:\text{Y}_2\text{SiO}_5$, in which we demonstrate storage of 6 temporal modes with mean photon occupation number $\mu_{\text{in}} = 0.711 \pm 0.006$ per mode for a duration of 20 ms using a XY-4 DD sequence with 4 pulses. The output signal-to-noise (SNR) ratio is 7.4 ± 0.5 , for an internal storage efficiency of $\eta_s = 7\%$, which excludes the contribution of losses due to the optical path between the memory output and the detector. These results represent a 40-fold increase in qubit storage time with respect to the longest photonic qubit storage in a solid-state device²⁶. The improvement in storage time is due to the application of a small magnetic field of 1.35 mT, see also^{24,29}, which increases the spin coherence time with more than an order of magnitude while simultaneously resulting in a Markovian spin diffusion that can be further suppressed by DD sequences. By applying a longer DD sequence of 16 pulses (XY-16) we demonstrate storage with $\mu_{\text{in}} = 1.062 \pm 0.007$ per mode for a duration of 100 ms, with a SNR of 2.5 ± 0.2 and an efficiency of $\eta_s = (2.60 \pm 0.02)\%$. In addition we stored two time-bin qubits for 20 ms and performed a quantum state tomography of the output state, showing a fidelity of $F = (85 \pm 2)\%$ for $\mu_{\text{in}} = 0.92 \pm 0.04$ photons per qubit. To analyze the qubit we propose a composite adiabatic control pulse that projects the output qubit on superposition states of the time-bin modes. The current limit in storage time is technical, due to heating effects in the cryo cooler caused by the high power of the DD pulses and the duty cycle of the sequence. The measured spin coherence time as a function of the DD pulse number n_p follows closely the expected $n_p^{2/3}$ dependence, which suggests that considerably longer storage times are within reach with some engineering efforts.

¹Département de Physique Appliquée, Université de Genève, Rue de l'École-de-Médecine 20, 1205 Genève, Switzerland. ²Université côte d'Azur, CNRS, Institut de Physique de Nice, Parc Valrose, Nice Cedex 2, France. ✉email: mikael.afzelius@unige.ch

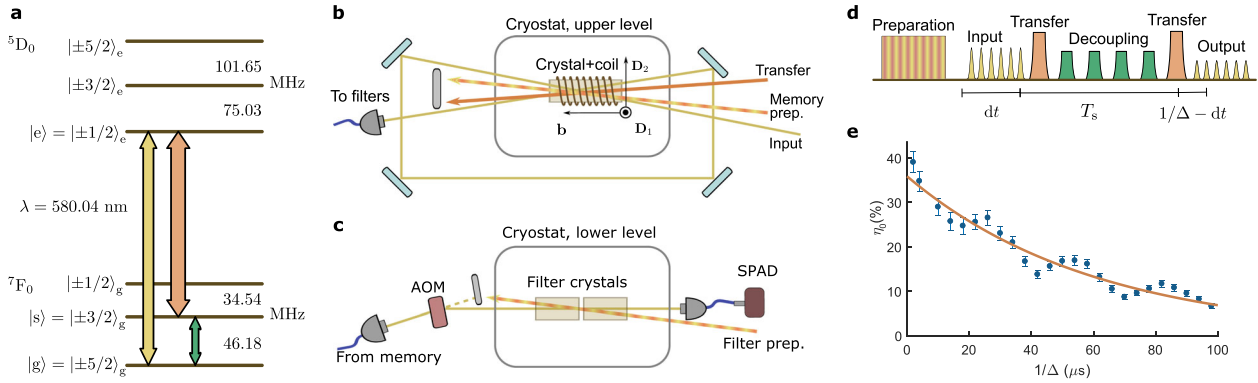


Fig. 1 System and setup. **a** Atomic energy structure of $^{151}\text{Eu}^{3+}:\text{Y}_2\text{SiO}_5$ and transitions used in the memory protocol. **b** and **c**, sketches of the experimental setup around the memory and filter crystals, respectively. The crystals are glued on a custom mount with two levels at different heights, in the same cryostat. The memory crystal is at the center of a small coil used to generate the RF signal. A larger coil (not shown) on top of the cryostat generates a static magnetic field along the \mathbf{D}_1 axis of the Y_2SiO_5 crystal. Optical beams are depicted with exaggerated angles for clarity. AOM: acousto-optic modulator; SPAD: single photon avalanche diode. **d** Sketch of the time sequence of pulses used for multimode spin-storage. **e** AFC efficiency measured as a function of AFC time $1/\Delta$, with bright input pulses and magnetic field of 1.35 mT along \mathbf{D}_1 . The solid line indicates the exponential fit resulting in zero-time efficiency $\eta_0 = (36 \pm 3)\%$ and effective coherence time $T_2^{\text{AFC}} = (240 \pm 30) \mu\text{s}$, see text for details. Error bars represent 95% confidence intervals. More information on the experimental setup and pulse sequences can be found in the Methods section and in Supplementary Notes 1 and 3.

RESULTS

The $^{151}\text{Eu}^{3+}:\text{Y}_2\text{SiO}_5$ system

The platform for our quantum memory is a $^{151}\text{Eu}^{3+}:\text{Y}_2\text{SiO}_5$ crystal with an energy structure at zero magnetic field as in Fig. 1a. The excited and ground states can be connected via optical transitions at about 580 nm³⁰. The quadrupolar interaction due to the effective nuclear spin $I = 5/2$ of the Eu^{3+} ions generates three doublets in both the ground and excited states, separated by tens of MHz. This structure allows to choose a Λ -system with a first ground state $|g\rangle$ into which the population is initialized, connected to an excited state $|e\rangle$ for optical absorption of the input light, and a second ground state $|s\rangle$ for on-demand long-time storage.

The full AFC-spin wave protocol^{7,31}, sketched in Fig. 1d, begins by initializing the memory so to have a comb-like structure in the frequency domain with periodicity Δ on $|g\rangle$ and an empty $|s\rangle$ state, via an optical preparation beam (see Fig. 1b). The initialization step closely follows the procedure outlined by Jobez et al.³². The photons to be stored are sent along the input path and are absorbed by the AFC on the $|g\rangle \leftrightarrow |e\rangle$ transition, leading to a coherent superposition in the atomic ensemble. The AFC results in a rephasing of the atoms after a duration $1/\Delta$, while normally they would dephase quickly due to the inhomogeneous broadening. Before the AFC echo emission, the excitation is transferred to the storage state $|s\rangle$ via a strong transfer pulse. The radio-frequency (RF) field at 46.18 MHz then dynamically decouples the spin coherence from external perturbations and compensates for the spin dephasing induced by the inhomogeneous broadening of the spin transition $|g\rangle \leftrightarrow |s\rangle$. In our particular crystal, the shape of the spin transition absorption line is estimated to be Gaussian with a width of about 60 kHz (Supplementary Note 2). A second strong optical pulse transfers the coherent atoms back into the $|e\rangle$ state, after which the AFC phase evolution concludes with an output emission along $|e\rangle \rightarrow |g\rangle$.

To implement the memory scheme, a coherent and powerful laser (1.8 W) at 580 nm is generated by amplifying and frequency doubling a 1160 nm laser that is locked on a high-finesse optical cavity³³. The 580 nm beam traverses a cascade of bulk acousto-optic modulators (AOM), each controlling an optical channel of the experiment, namely optical transfer, memory preparation, filter preparation and input. The optical beams and the main

elements of the setup are represented in Fig. 1b, c. A memory and two filtering crystals are cooled down in the same closed-cycle helium cryostat to ~ 4 K, placed on two levels of a single custom mount. The 1.2 cm long memory crystal is enveloped by a coil of the same length to generate the RF field. Another larger coil is placed outside the cold chamber and used to generate a static magnetic field. After the cryostat, the light in the input path can be detected either by a linear Si photodiode for experiments with bright pulses, or by a Si single photon avalanche diode (SPAD) detector for weak pulses at the single photon-level. For photon counting it is necessary to use a filtering setup (Fig. 1c) to block any scattered light and noise generated by the second transfer pulse. Another AOM acts as a temporal gate, before passing the beam through two filtering crystals that are optically pumped so to have a transmission window around the input photon frequency and maximum absorption corresponding to the transfer pulse transition.

The $^{151}\text{Eu}^{3+}:\text{Y}_2\text{SiO}_5$ crystals are exposed to a small static magnetic field along the crystal \mathbf{D}_1 axis³⁴. At zero magnetic field, the protocol enabled to achieve storage of multiple coherent single photon-level pulses up to about 1 ms²⁶. However, it has been shown that even a weak magnetic field can increase the coherence lifetime^{19,24,35,36}, which motivated us to use a ~ 1.35 mT field along the \mathbf{D}_1 axis²⁹.

Spin-wave AFC

The AFC spin-wave memory consists of three distinct processes: the AFC echo, the transfer pulses and the RF sequence, and each process introduces a set of parameters that will need to be optimized globally in order to achieve the best possible SNR, multimode capacity and storage time. Below we briefly describe some of the constraints leading to the particular choice of parameters used in these experiments.

The maximum AFC spin-wave efficiency is limited by the AFC echo efficiency for a certain $1/\Delta$, which typically decreases exponentially as a function of $1/\Delta$. We can define an effective AFC coherence lifetime T_2^{AFC} and efficiency η_{AFC} as $\eta_{\text{AFC}} = \eta_0 \exp(-4/(\Delta T_2^{\text{AFC}}))$ ³², where η_0 depends on the optical depth and the AFC parameters. With an external magnetic field of 1.35 mT $\parallel \mathbf{D}_1$, we obtained $T_2^{\text{AFC}} = (240 \pm 30) \mu\text{s}$ with an extrapolated zero-time efficiency of $\eta_0 = (36 \pm 3)\%$, see Fig. 1e. The η_0 efficiency is consistent with the initial optical depth of 6 in our

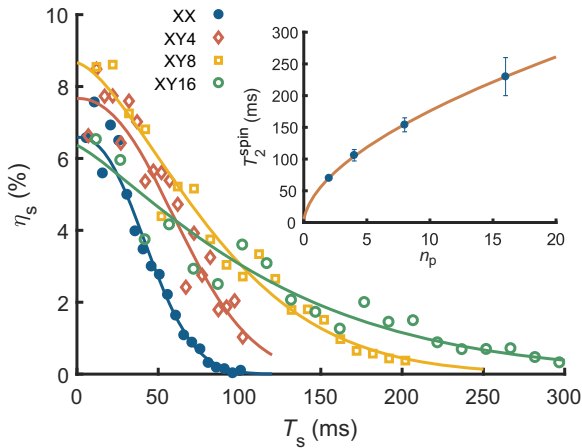


Fig. 2 Spin storage coherence time. Spin storage efficiency as a function of storage time for four different dynamical decoupling sequences. The solid lines are fits of the Mims model with $\eta_s(0)$, T_2^{spin} and m as free parameters (see text for details). Inset: spin effective coherence time as a function of the number of pulses n_p in the DD sequence. The solid line is a fit to a power law as described in the main text. Error bars indicate a 95% confidence interval. See Supplementary Table 1 for details on the T_2^{spin} data.

double-pass input configuration (each pass provides an optical depth of about 3). The effect of the field-induced Zeeman split on the AFC preparation process is discussed in detail ref. ²⁹. In short no adverse effects of the comb quality is expected when the comb periodicity is a multiple of the excited state splitting, provided more than two ground states are available for optical pumping as in $\text{Eu}^{3+}:\text{Y}_2\text{SiO}_5$, while other periodicities can lead to a lower AFC efficiency. In Fig. 1e the modulation period of about $25 \mu\text{s}$ indeed corresponds to the excited state splitting of 41.4 kHz . The exponential decay implies that there is a trade-off between the memory efficiency (favoring short $1/\Delta$) and temporal multi-mode capacity (favoring long $1/\Delta$). In addition we must consider the shortest input duration that can be stored, which is limited by the effective memory bandwidth.

The optical transfer pulses should ideally perform a perfect coherent population inversion between states $|e\rangle$ and $|s\rangle$, uniformly over the entire bandwidth of the input pulse. Efficient inversion with a uniform transfer probability in frequency space can be achieved by adiabatic, chirped pulses³⁷. Here we employ two HSH pulses proposed by Tian et al.³⁸, which are particularly efficient given a limitation in pulse duration. For a fixed Rabi frequency the bandwidth of the pulse can be increased by increasing the pulse duration³⁷, which however reduces the multimode capacity of the AFC spin-wave memory.

Considering as a priority to preserve the storage efficiency while still being able to store several time modes, we set $1/\Delta = 25 \mu\text{s}$, corresponding to the first maximum (with efficiency 28%) on the AFC echo decay curve in Fig. 1e. Given the $1/\Delta$ delay, we optimized the HSH control pulse duration, leading to a bandwidth of 1.5 MHz for a HSH pulse duration of $15 \mu\text{s}$. The remaining $10 \mu\text{s}$ were used to encode six temporal modes, giving a mode duration of $T_m = 1.65 \mu\text{s}$. Each mode contained a Gaussian pulse with a full-width at half-maximum of about 700 ns .

The RF sequence compensates for the inhomogeneous spin dephasing and should ideally reduce the spectral diffusion due to spin-spin interactions through DD^{24,39–41}. However, effective dynamical decoupling requires many pulses, with pulse separations less than the characteristic time of the spin fluctuations. Pulse errors can then introduce noise at the memory output²⁶, which in principle can be reduced by using error-compensating DD sequences²⁷. In practice, however, other factors such as

heating of the crystal due to the intense RF pulses limit the effectiveness of such sequences, and noise induced by the RF sequence is the main limitation in SNR of long-duration AFC spin-wave memories^{9,26,42}.

Characterization with bright pulses

We first present a characterization of the memory using bright input pulses and a linear Si photodiode, implementing four decoupling sequences with a number of pulses ranging from a minimum of 2 to a maximum of 16. Figure 2 displays the resulting efficiency decay curves as a function of the time T_s spent by the atoms in the spin transition, which corresponds to the time difference between the two optical transfer pulses. The solid lines show fits obtained from a Mims model, which takes into account the effect of spectral diffusion⁴³ according to the relation $\eta_s(T_s) = \eta_s(0) \exp[-2(T_s/T_2^{\text{spin}})^m]$, where T_2^{spin} is the effective spin coherence time, and m the Mims factor. More details can be found in Supplementary Note 3.

We extracted effective coherence times of 70 ± 2 , 106 ± 9 , 154 ± 11 , and $(230 \pm 30) \text{ ms}$ respectively for XX, XY-4, XY-8, and XY-16 sequences, which show a clear decoupling effect as more pulses are added. This is also confirmed by the expected change of T_2^{spin} as a function of n_p visible in the inset of Fig. 2, which closely follows a power-law relation $T_2^{\text{spin}}(n_p) = T_2^{\text{spin}}(1) n_p^{\gamma_p}$ with $\gamma_p = 0.57 \pm 0.03$ and $T_2^{\text{spin}}(1) = (47 \pm 2) \text{ ms}$ as expected for an Ornstein-Uhlenbeck spectral diffusion process^{40,41,44}. A similar scaling was obtained in Holzäpfel et al.²⁴, using a slightly different experimental setup, magnetic field and Λ -system, which indicates that much longer storage times could be achieved. However, adding more pulses for the same storage times introduces additional heating, causing temperature-dependent frequency shifts of the optical transition^{30,45}. This technical issue could be addressed in the future by optimizing the heat dissipation in proximity of the crystal. The extrapolated zero-time efficiencies vary between 6% and 9%, and the data appear relatively scattered around the fitted curves for the longer decoupling sequences. These two observations might be a sign of the presence of beats originating in the different phase paths available to the atoms during storage, due to the small Zeeman splitting of the ground state doublets in this regime of weak magnetic field. Similar effects have been shown in a more detailed model of interaction between a system with splittings smaller than the RF pulses chirp²⁹.

Single-photon level performance

We now discuss the memory performance at the single photon level. The dark histograms in Fig. 3 show three examples of spin storage outputs with their respective input modes for reference. The lighter histograms show the noise background, measured while executing the complete memory scheme without any input light (see Methods section for details). This noise floor, when integrated over the mode size $T_{m,r}$, gives us the noise probability p_N . When compared to the sum of the counts in the retrieved signal in the mode, the summed noise count is well below the retrieved signal for all the storage times here reported. We used an XY-4 type of RF sequence for storage at 20 ms, XY-8 for 50 ms, and XY-16 for 100 ms. Table 1 summarizes the relevant results, in particular with SNR values ranging from 7.4 to 2.5 for 20 ms and 100 ms respectively. The average input photon number per time mode μ_{in} is close to 1 in all cases, although it varies slightly. To account for this, an independent figure of merit is the parameter $\mu_1 = p_N/\eta$, which corresponds to the average input photon number that would give an SNR of 1 in output⁴⁶. Since it scales as the inverse of the efficiency²⁶, it increases with storage time, but for all cases studied here it is well below 1.

The noise probability p_N varied from $7 \cdot 10^{-3}$ to $11 \cdot 10^{-3}$, see Table 1, similar to previous experiments²⁶. An independent noise measurement at 20 ms showed that the XX, XY-4, and XY-8

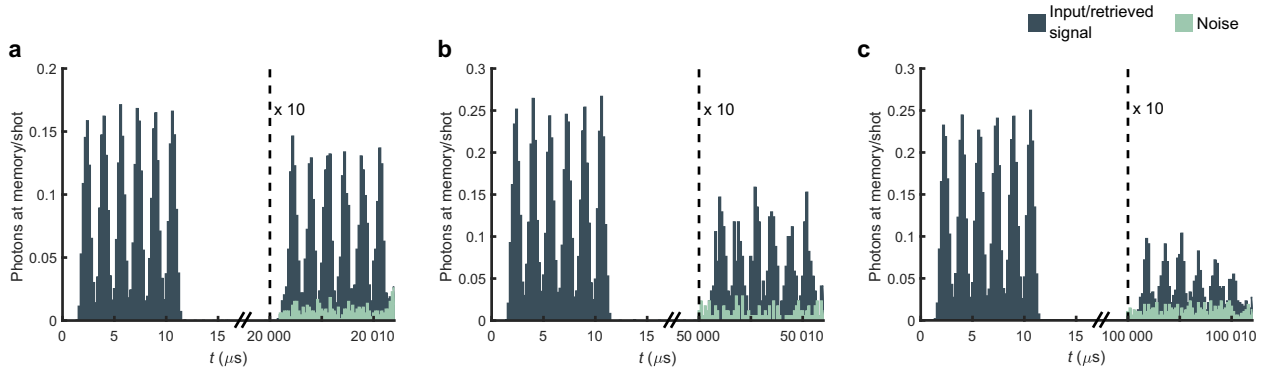


Fig. 3 Single photon-level spin storage. Examples of spin storage at 20 ms (a), 50 ms (b), and 100 ms (c). The dark blue histogram shows the input pulses (left of each figure) and the retrieved signal. Light green histograms display the noise floor. Each signal peak is a center of a $1.65 \mu\text{s}$ time mode. The measured mean photon number in each input mode was close to 1, within the statistical variations. The mean photon number averaged over all six modes is given in Table 1. See Methods and Supplementary Tables 2, 3, and 5 for more details.

T_s (ms)	μ_{in}	p_N	η (%)	SNR	μ_1
20	0.711 ± 0.006	0.0073 ± 0.0012	7.39 ± 0.04	7.4 ± 0.5	0.098 ± 0.002
50	1.21 ± 0.01	0.009 ± 0.002	4.37 ± 0.04	5.6 ± 0.7	0.218 ± 0.008
100	1.062 ± 0.007	0.0110 ± 0.0015	2.60 ± 0.02	2.5 ± 0.2	0.445 ± 0.008

Values of input mean photon number μ_{in} , storage efficiency η , signal-to-noise ratio SNR and the equivalent mean input photon number for SNR = 1, μ_1 , for different spin-wave storage times T_s . The reported values are averages over the six temporal modes, and the value for each mode stems from the summed counts over the mode size T_m . See Methods and Supplementary Tables 2, 3, and 5 for more details.

resulted in almost identical noise values of $p_N = 7.4 \cdot 10^{-3}$, $8.1 \cdot 10^{-3}$ and $8.6 \cdot 10^{-3}$ (error $\pm 0.3 \cdot 10^{-3}$), respectively. This shows that pulse area errors are effectively suppressed by the higher order DD sequences, and that the read-out noise is caused by other types of errors, which at this point are not well understood.

If compared with the efficiencies measured with bright pulses in Fig. 2, the storage efficiency measured at the single photon-level is noticeably lower for 50 and 100 ms. We believe this is due to the long measurement times required for accumulating the necessary statistics, which exposes the experiment to long-term fluctuations affecting optical alignment in general and specifically fiber coupling efficiencies. Nonetheless, our results show that our memory is capable of storing successfully multiple time modes at the single photon level, with a SNR that is in principle compatible with storage of quantum states²⁶ for up to 100 ms. More information on the memory parameter estimations from the data can be found in Supplementary Table 2.

Time-bin qubit storage

To characterize the quantum fidelity of the memory, we analyzed the storage of time-bin-encoded qubits. Both qubits were prepared in the ideally pure superposition state $\psi_{in} = 1/\sqrt{2}(|E\rangle + |L\rangle)$, where $|E\rangle$ and $|L\rangle$ represent the early and late time modes of each qubit. Exploiting our six-modes capacity, we encoded the components $|E\rangle$ and $|L\rangle$ of the first qubit into the temporal modes 2 and 3, respectively, and similarly for the second qubit in modes 5 and 6.

To perform a full quantum tomography of the memory output state, represented by the density matrix ρ_{out} , one needs to be able to perform measurements of the observables represented by the Pauli matrices σ_x , σ_y and σ_z . The observable σ_z can simply be measured using histogram traces as shown in Fig. 3. The σ_x and σ_y observables can be measured by making two partial read-outs of the memory^{46–48}, separated by the qubit mode spacing T_m , where each partial transfer pulse should ideally perform a 50% transfer as

both modes are emitted after the second transfer pulse. In the past, this has been achieved by using two distinct, shorter transfer pulses^{46,48,49}, separated by T_m , which in practice can reduce the efficiency below the ideal 50% transfer⁴⁶. This is particularly true for long adiabatic, chirped pulses, which would then need to be severely shortened to produce two distinct pulses separated by the mode spacing T_m . In addition the first control pulse would need to be reduced in duration as well, as the chirp rate of all the transfer pulses should be the same³⁷.

To overcome the efficiency limitation for qubit analysis based on partial read-outs with adiabatic pulses, we propose a composite pulse that can achieve the ideal 50% partial transfer, independently of the pulse duration and mode separation. The composite HSH pulse (cHSH) is a linear sum of two identical adiabatic HSH pulses, with their centers separated in time by T_m . The cHSH has a characteristic amplitude oscillation due to the interference of the two chirps, see Fig. 4a. Intuitively, one can think of each specific frequency within the AFC bandwidth as being addressed twice by the cHSH, once by each component, at two distinct times separated exactly by T_m , despite the fact that the whole cHSH pulse itself is much longer than T_m . As a consequence, the addressed atomic population partially rephases after the pulse at two times separated by T_m . An alternative method for analyzing qubits consists in using an AFC-based analyzer in the filtering crystals^{50,51}. However, we observed that the SNR was deteriorated when using the same crystals as both filtering and analyzing device. The cHSH-based analyzer resulted in a significantly better SNR after the filters, yielding a higher storage fidelity.

The phase difference θ between the two cHSH components sets the measurement basis, where $\theta = 0$ ($\theta = \pi/2$) and $\theta = \pi$ ($\theta = 3\pi/2$) projects respectively on the $|+\rangle$ and $|-\rangle$ eigenstates of σ_x (σ_y), encoded in the early-late time modes basis as $1/\sqrt{2}(|E\rangle + e^{i\theta}|L\rangle)$. Note that this type of analyzer can only project onto one eigenstate of each basis, hence two measurements are required

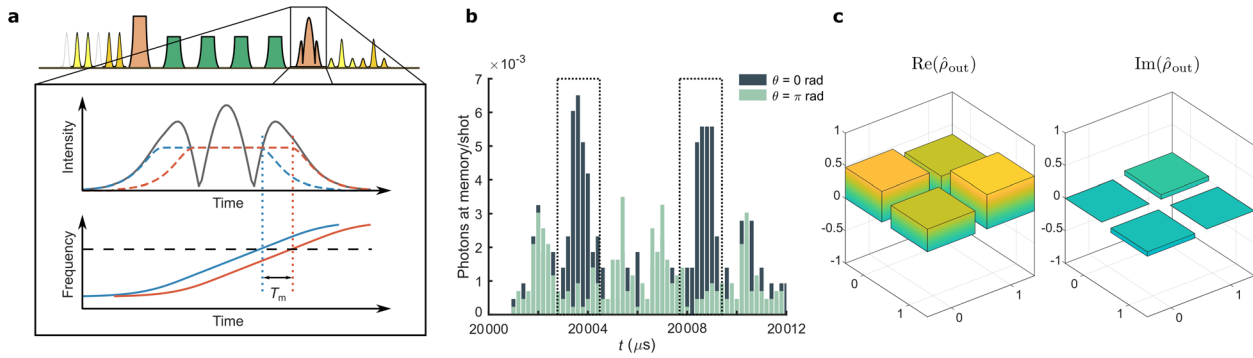


Fig. 4 Qubit tomography. **a** Projections for the tomography are implemented by choosing the appropriate pulse profile for the second transfer pulse in the storage sequence. For projections in σ_x and σ_y the second transfer pulse takes the form of a composite HSH, obtained from the sum of the fields of two chirped pulses that are temporally shifted by the width of one time bin (T_m) relatively to each other. In the top figure, the envelopes of the two partial pulses are shown with dashed lines and the resulting composite pulse with a solid line. As a consequence, each specific frequency of the AFC (e.g., the dashed line in the bottom figure) is addressed at two different times separated by T_m , as indicated by the crossings with the two solid lines. **b** Two examples of projection of the output state onto $|+\rangle$ (dark histogram) and $|-\rangle$ (light histogram) eigenstates of the σ_x operator. The overlap is proportional to the amplitude in the interference bins (dotted boxes). The input state ψ_{in} was prepared in the $|+\rangle$ eigenstate of σ_x . **c** Reconstructed density matrix $\hat{\rho}_{out}$ of the output state. See Supplementary Note 4 for more details.

per Pauli operator. Figure 4b shows the histograms corresponding to the two σ_x projections.

After measuring the expectation value of all three Pauli operators, we can reconstruct the full quantum state $\hat{\rho}_{out}$ using direct inversion⁵², after verifying that the corresponding state matrix is indeed physical. We hence derive a fidelity of $F = (85 \pm 2)\%$, averaged over the two qubits. Raw counts and the resulting expectation values can be found in Supplementary Table 4, with corresponding numbers of experiment repetitions in Supplementary Table 6. The average number of photons per qubit was $\mu_{in} = 0.92 \pm 0.04$ and the reconstructed density matrix $\hat{\rho}_{out}$ is shown in Fig. 4c. The purity of the reconstructed state is $P = (76 \pm 3)\%$, which limits the maximum achievable fidelity in absence of any unitary errors to 87%. This indicates that the fidelity is limited by white noise generated by the RF sequence at the memory read-out. Another element supporting this conclusion is given by the fidelity measured with bright pulses, so that the noise is negligible (see Supplementary Note 4), yielding a value of 96%. We further note that the σ_z measurement yielded a SNR of 3.48 ± 0.15 , which when scaled up to the single photon level in one time bin becomes about 7.0. This is compatible with the value reported in Table 1 and would result in an upper bound on the fidelity of $F = (\text{SNR} + 1)/(\text{SNR} + 2) = (88.9 \pm 0.04)\%$ assuming a white noise model²⁶.

The measured qubit fidelity can be compared to different criteria for quantum storage. In this work we characterize the memory by storing qubits encoded onto weak coherent states. In this context Specht et al.⁵³ introduced a classical fidelity limit by comparing to a measure-and-prepare strategy, where the memory inefficiency and multiphoton components of the states are exploited. Nevertheless, for the efficiency of 7.39% and the mean qubit photon number of $\mu_{in} = 0.92$ the criterion gives a maximum classical fidelity of 81.2% (see Supplementary Note 4), such that our qubit fidelity at 20 ms surpasses the classical limit. We can also consider future applications of the memory in terms of storing a qubit encoded onto a true single photon (Fock state), for which the classical limit is $F = 2/3$ ⁵⁴. For storage of true single photon qubits it can be shown that this limit can be surpassed provided that the probability p of finding the photon before the memory is larger than the μ_1 parameter (see Table 1)^{9,26}. Recent quantum memory experiments in praseodymium-doped Y_2SiO_5 has reached a heralding efficiency of 19% of finding a true single photon before the memory⁵⁵, which with our $\mu_1 = 0.098$ at 20 ms storage time would result in a theoretical qubit fidelity of about 75%. The

fidelity can be improved by a combination of increasing current memory efficiency and single-photon heralding efficiency.

DISCUSSION

The results presented here demonstrate that long-duration quantum storage based on dynamical decoupling of spin-wave states in $^{151}\text{Eu}^{3+}:\text{Y}_2\text{SiO}_5$ is a promising avenue. In terms of qubit storage, we observe a 40-fold increase in storage time with respect to the previous longest quantum storage of photonic qubits in a solid-state device⁹. Currently, the storage time in $^{151}\text{Eu}^{3+}:\text{Y}_2\text{SiO}_5$ is limited by the heating observed when adding more pulses in the decoupling sequence, which is a technical limitation, but the classical storage experiments by Holzäpfel et al.²⁴ suggest that even longer storage times are within reach in $^{151}\text{Eu}^{3+}:\text{Y}_2\text{SiO}_5$. Solving the heating problem will also allow applying DD pulses in a rapid succession with fixed time separation, as done by Holzäpfel et al.²⁴, giving more flexibility in the read-out time and reducing any deadtime of the memory. In general the implications of the timing of DD sequences have not yet been addressed in rate calculations of quantum repeaters. Our observation that DD sequences with more pulses did not generate more read-out noise is key to achieving longer storage times also at the quantum level. We also note that these techniques could be applied also to Pr^{3+} doped Y_2SiO_5 crystals, where currently quantum entanglement storage experiments are limited to about $50 \mu\text{s}$ ⁵⁶. Another interesting avenue is to apply these techniques to extend the storage time of spin-photon correlations experiments^{42,51} in rare-earth-doped crystals.

METHODS

Expanded setup

The core of the setup consist of a closed-cycle pulsed helium cryostat with a sample chamber at a typical temperature of 3.5 K. In the sample chamber, a custom copper mount holds the memory crystal, with dimensions $2.5 \times 2.9 \times 12.3 \text{ mm}$ along the ($\mathbf{D}_1, \mathbf{D}_2, \mathbf{b}$) axes³⁴, and a series of two filtering crystals with similar size. All these are $^{151}\text{Eu}^{3+}:\text{Y}_2\text{SiO}_5$ crystals with a doping concentration of 1000 ppm²⁶. Around the memory crystal, a copper coil generates the RF field to manipulate the atoms on their spin transitions. The coil is coupled to a resonator circuit, with resonance tuned on the 46 MHz spin transition, which produces a Rabi frequency of 120 kHz, corresponding roughly to an AC field of amplitude 12 mT. Before the resonator, the RF signal is created by an arbitrary wave generator, and amplified with a 100 W amplifier coupled to a circulator to redirect unwanted reflection from the resonator system.

The input beam is used to create the optical pulses to be stored, and it goes through the memory crystal twice with a waist diameter of 50 μm . The memory preparation beam is overlapped with the input path with a larger spot size around 700 μm , to ensure homogeneity of the preparation along the crystal length, with an incident angle of about 1° . The transfer beam is overlapped in a similar way, with a beam diameter at the waist of 250 μm .

The AFC structure is prepared with a 3 MHz total spectral width, which however is not fully exploited since the 1.5 MHz bandwidth of the HSH transfer pulses limits the effective memory bandwidth. The width of the transparency and absorption windows in the filter crystals were of 2 MHz, with a total optical depth of ~ 7.4 in the absorption window through the two crystals. The relative spectral extinction ratio should thus be $\exp(7.4) : 1 = 1636 : 1$.

More information on the setup can be found in Supplementary Notes 1 and 2.

Photon counting and noise measurement

The quantities μ_{in} and p_{N} in Table 1, correspond to average number of photons at the memory output for a single storage attempt. They are obtained by summing raw detections in modes of duration $T_{\text{m}} = 1.65 \mu\text{s}$, then dividing by the number of experiment repetitions, averaging over the 6 modes, and dividing by the detector efficiency $\eta_{\text{D}} = 57\%$ and cryostat-to-detector path transmission (typically between 17% and 20%). The histograms in Figs. 3 and 4b are obtained in the same way for a binning resolution of 200 ns.

Noise photons at the memory read-out originate from excitation of ions from the $|g\rangle$ state to the $|s\rangle$ state during the DD sequence, due to imperfections of the RF pulses^{26,27}. These ions are then excited by the read-out transfer pulse and decay on the $|e\rangle$ - $|g\rangle$ transition through spontaneous emission. These noise photons are thus spectrally indistinguishable from the stored photons. The spontaneous character was verified by observing that its decay constant corresponds to the radiative lifetime T_1 . Note that without RF manipulation the read-out noise is significantly reduced, i.e., the main SNR limitation in current spin-wave experiments is due to RF-induced photon noise.

The noise parameter p_{N} indicates the probability of a noise photon being emitted by the memory during a time corresponding to the mode size $T_{\text{m}} = 1.65 \mu\text{s}$. For the spin storage data at $T_{\text{s}} = 20 \text{ms}$, visible in Fig. 3a and Table 1, it is measured independently by blocking the input beam during the full storage sequence in the same time modes in which the retrieved modes would be. A more detailed analysis per-mode and the exact number of repetitions for all experiments are reported respectively in Supplementary Tables 3 and 5.

To decrease the total acquisition time of the experiments at $T_{\text{s}} = 50$ and 100 ms, we calculated the respective p_{N} values reported in Table 1 from a $\sim 225 \mu\text{s}$ time window centered at about 190 μs after the first retrieved mode in the same dataset. By doing so, we exploited the fact that the noise floor is due to spontaneous emission with a decay time of 1.9 ms¹⁹, and can be considered uniform up to $\sim 200 \mu\text{s}$ after readout. This is confirmed experimentally on the 20 ms datasets, as the difference in p_{N} calculated in the retrieved mode position of the data with input blocked correspond to the result of the procedure above within the Poissonian standard deviation. The histograms displaying noise in Fig. 3b, c are representative regions of the noise floor taken at about 20 μs after the retrieved modes in the same dataset.

All errors are estimated from Poissonian standard deviations on the raw detector counts and propagated considering the memory temporal modes as independent.

DATA AVAILABILITY

The data sets generated and/or analyzed during the current study are available from the corresponding authors upon reasonable request.

Received: 14 September 2021; Accepted: 10 February 2022;

Published online: 15 March 2022

REFERENCES

1. Briegel, H.-J., Dür, W., Cirac, J. I. & Zoller, P. Quantum repeaters: the role of imperfect local operations in quantum communication. *Phys. Rev. Lett.* **81**, 5932–5935 (1998).

2. Duan, L.-M., Lukin, M. D., Cirac, J. I. & Zoller, P. Long-distance quantum communication with atomic ensembles and linear optics. *Nature* **414**, 413–418 (2001).
3. Sangouard, N., Simon, C., de Riedmatten, H. & Gisin, N. Quantum repeaters based on atomic ensembles and linear optics. *Rev. Mod. Phys.* **83**, 33–80 (2011).
4. Kimble, H. J. The quantum internet. *Nature* **453**, 1023–1030 (2008).
5. Cabrillo, C., Cirac, J. I., García-Fernández, P. & Zoller, P. Creation of entangled states of distant atoms by interference. *Phys. Rev. A* **59**, 1025–1033 (1999).
6. Nunn, J. et al. Multimode memories in atomic ensembles. *Phys. Rev. Lett.* **101**, 260502–4 (2008).
7. Afzelius, M., Simon, C., de Riedmatten, H. & Gisin, N. Multimode quantum memory based on atomic frequency combs. *Phys. Rev. A* **79**, 052329 (2009).
8. Sinclair, N. et al. Spectral multiplexing for scalable quantum photonics using an atomic frequency comb quantum memory and feed-forward control. *Phys. Rev. Lett.* **113**, 053603 (2014).
9. Laplane, C. et al. Multiplexed on-demand storage of polarization qubits in a crystal. *New J. Phys.* **18**, 013006 (2015).
10. Parniak, M. et al. Wavevector multiplexed atomic quantum memory via spatially-resolved single-photon detection. *Nat. Commun.* **8**, 1–9 (2017).
11. Yang, T.-S. et al. Multiplexed storage and real-time manipulation based on a multiple degree-of-freedom quantum memory. *Nat. Commun.* **9**, 1–8 (2018).
12. Heller, L., Farrera, P., Heinze, G. & de Riedmatten, H. Cold-atom temporally multiplexed quantum memory with cavity-enhanced noise suppression. *Phys. Rev. Lett.* **124**, 210504 (2020).
13. Simon, C. et al. Quantum repeaters with photon pair sources and multimode memories. *Phys. Rev. Lett.* **98**, 190503 (2007).
14. Usmani, I., Afzelius, M., de Riedmatten, H. & Gisin, N. Mapping multiple photonic qubits into and out of one solid-state atomic ensemble. *Nat. Commun.* **1**, 12 (2010).
15. Seri, A. et al. Quantum correlations between single telecom photons and a multimode on-demand solid-state quantum memory. *Phys. Rev. X* **7**, 021028 (2017).
16. Seri, A. et al. Quantum storage of frequency-multiplexed heralded single photons. *Phys. Rev. Lett.* **123**, 080502 (2019).
17. Sabooni, M., Li, Q., Kröll, S. & Rippe, L. Efficient quantum memory using a weakly absorbing sample. *Phys. Rev. Lett.* **110**, 133604 (2013).
18. Hedges, M. P., Longdell, J. J., Li, Y. & Sellars, M. J. Efficient quantum memory for light. *Nature* **465**, 1052–1056 (2010).
19. Equall, R. W., Sun, Y., Cone, R. L. & Macfarlane, R. M. Ultraslow optical dephasing in $\text{Eu}^{3+}:\text{Y}_2\text{SiO}_5$. *Phys. Rev. Lett.* **72**, 2179 (1994).
20. Equall, R. W., Cone, R. L. & Macfarlane, R. M. Homogeneous broadening and hyperfine structure of optical transitions in $\text{Pr}^{3+}:\text{Y}_2\text{SiO}_5$. *Phys. Rev. B* **52**, 3963 (1995).
21. Heinze, G., Hubrich, C. & Halfmann, T. Stopped light and image storage by electromagnetically induced transparency up to the regime of one minute. *Phys. Rev. Lett.* **111**, 033601 (2013).
22. Zhong, M. et al. Optically addressable nuclear spins in a solid with a six-hour coherence time. *Nature* **517**, 177–180 (2015).
23. Businger, M. et al. Optical spin-wave storage in a solid-state hybridized electron-nuclear spin ensemble. *Phys. Rev. Lett.* **124**, 053606 (2020).
24. Holzäpfel, A. et al. Optical storage for 0.5 s in a solid-state atomic frequency comb memory using dynamical decoupling. *New J. Phys.* **22**, 063009 (2020).
25. Wu, Y., Liu, J. & Simon, C. Near-term performance of quantum repeaters with imperfect ensemble-based quantum memories. *Phys. Rev. A* **101**, 042301 (2020).
26. Jobez, P. et al. Coherent spin control at the quantum level in an ensemble-based optical memory. *Phys. Rev. Lett.* **114**, 230502 (2015).
27. Zambrini Cruzeiro, E., Fröwis, F., Timoney, N. & Afzelius, M. Noise in optical quantum memories based on dynamical decoupling of spin states. *J. Mod. Opt.* **63**, 2101–2113 (2016).
28. Fraval, E., Sellars, M. J. & Longdell, J. J. Method of extending hyperfine coherence times in $\text{Pr}^{3+}:\text{Y}_2\text{SiO}_5$. *Phys. Rev. Lett.* **92**, 077601–4 (2004).
29. Etesse, J., Holzäpfel, A., Ortu, A. & Afzelius, M. Optical and spin manipulation of non-kramers rare-earth ions in a weak magnetic field for quantum memory applications. *Phys. Rev. A* **103**, 022618 (2021).
30. König, F. et al. Temperature and concentration dependence of optical dephasing, spectral-hole lifetime, and anisotropic absorption in $\text{Eu}^{3+}:\text{Y}_2\text{SiO}_5$. *Phys. Rev. B* **68**, 085109 (2003).
31. Afzelius, M. et al. Demonstration of atomic frequency comb memory for light with spin-wave storage. *Phys. Rev. Lett.* **104**, 040503 (2010).
32. Jobez, P. et al. Towards highly multimode optical quantum memory for quantum repeaters. *Phys. Rev. A* **93**, 032327 (2016).
33. Jobez, P. et al. Cavity-enhanced storage in an optical spin-wave memory. *New J. Phys.* **16**, 083005 (2014).
34. Li, C., Wyon, C. & Moncorge, R. Spectroscopic properties and fluorescence dynamics of Er^{3+} and Yb^{3+} in Y_2SiO_5 . *IEEE J. Quantum Electron.* **28**, 1209–1221 (1992).

35. Alexander, A. L., Longdell, J. J. & Sellars, M. J. Measurement of the ground-state hyperfine coherence time of $^{151}\text{Eu}^{3+}:\text{Y}_2\text{SiO}_5$. *J. Opt. Soc. Am. B* **24**, 2479–2482 (2007).
36. Arcangeli, A., Lovrić, M., Tumino, B., Ferrier, A. & Goldner, P. Spectroscopy and coherence lifetime extension of hyperfine transitions in $^{151}\text{Eu}^{3+}:\text{Y}_2\text{SiO}_5$. *Phys. Rev. B* **89**, 184305 (2014).
37. Minář, J., Sangouard, N., Afzelius, M., de Riedmatten, H. & Gisin, N. Spin-wave storage using chirped control fields in atomic frequency comb-based quantum memory. *Phys. Rev. A* **82**, 042309 (2010).
38. Tian, M., Chang, T., Merkel, K. D. & Randall, W. Reconfiguration of spectral absorption features using a frequency-chirped laser pulse. *Appl. Opt.* **50**, 6548–6554 (2011).
39. Viola, L. & Lloyd, S. Dynamical suppression of decoherence in two-state quantum systems. *Phys. Rev. A* **58**, 2733–2744 (1998).
40. de Lange, G., Wang, Z. H., Ristè, D., Dobrovitski, V. V. & Hanson, R. Universal dynamical decoupling of a single solid-state spin from a spin bath. *Science* **330**, 60–63 (2010).
41. Medford, J. et al. Scaling of dynamical decoupling for spin qubits. *Phys. Rev. Lett.* **108**, 086802 (2012).
42. Cyril, L., Jobez, P., Etesses, J., Gisin, N. & Afzelius, M. Multimode and long-lived quantum correlations between photons and spins in a crystal. *Phys. Rev. Lett.* **118**, 210501 (2017).
43. Mims, W. B. Phase memory in electron spin echoes, lattice relaxation effects in $\text{CaWO}_4:\text{Er}$, Ce , Mn . *Phys. Rev.* **168**, 370 (1968).
44. Klauder, J. R. & Anderson, P. W. Spectral diffusion decay in spin resonance experiments. *Phys. Rev.* **125**, 912–932 (1962).
45. Thorpe, M. J., Leibbrandt, D. R. & Rosenband, T. Shifts of optical frequency references based on spectral-hole burning in $\text{Eu}^{3+}:\text{Y}_2\text{SiO}_5$. *New J. of Phys.* **15**, 033006 (2013).
46. Gündoğan, M., Ledingham, P. M., Kutluer, K., Mazzera, M. & de Riedmatten, H. Solid state spin-wave quantum memory for time-bin qubits. *Phys. Rev. Lett.* **114**, 230501 (2015).
47. Staudt, M. et al. Fidelity of an optical memory based on stimulated photon echoes. *Phys. Rev. Lett.* **98**, 113601–4 (2007).
48. Gündoğan, M., Mazzera, M., Ledingham, P. M., Cristiani, M. & de Riedmatten, H. Coherent storage of temporally multimode light using a spin-wave atomic frequency comb memory. *New J. Phys.* **15**, 045012 (2013).
49. Ma, Y.-Z. et al. Elimination of noise in optically rephased photon echoes. *Nat. Commun.* **12**, 4378 (2021).
50. Jobez, P. Stockage Multimode au Niveau Quantique Pendant une Milliseconde, Ph.D. thesis, <https://nbn-resolving.org/urn:nbn:ch:unige-836717> (2015).
51. Kutluer, K. et al. Time entanglement between a photon and a spin wave in a multimode solid-state quantum memory. *Phys. Rev. Lett.* **123**, 030501 (2019).
52. Schmied, R. Quantum state tomography of a single qubit: comparison of methods. *J. Mod. Opt.* **63**, 1744–1758 (2016).
53. Specht, H. P. et al. A single-atom quantum memory. *Nature* **473**, 190–193 (2011).
54. Massar, S. & Popescu, S. Optimal extraction of information from finite quantum ensembles. *Phys. Rev. Lett.* **74**, 1259–1263 (1995).
55. Lago-Rivera, D., Grandi, S., Rakonjac, J. V., Seri, A. & de Riedmatten, H. Telecom-heralded entanglement between multimode solid-state quantum memories. *Nature* **594**, 37–40 (2021).
56. Rakonjac, J. V. et al. Entanglement between a telecom photon and an on-demand multimode solid-state quantum memory. *Phys. Rev. Lett.* **127**, 210502 (2021).

ACKNOWLEDGEMENTS

We acknowledge funding from the Swiss FNS NCCR program Quantum Science Technology (QSIT), European Union Horizon 2020 research and innovation program within the Flagship on Quantum Technologies through GA 820445 (QIA) and under the Marie Skłodowska-Curie program through GA 675662 (QCALL). We also thank Philippe Goldner and Alban Ferrier from Chimie ParisTech for fruitful discussions and for providing the crystals.

AUTHOR CONTRIBUTIONS

A.O., J.E., and M.A. conceived and planned the experiments, which were mainly carried out by A.O. and A.H. A.O. set up most of the experiment, with contributions from J.E., and carried out the quantum memory characterization. A.H. implemented the qubit analysis method, with contributions from A.O. The manuscript was mainly written by A.O. and M.A., with contributions from all the authors. M.A. provided overall oversight of the project.

COMPETING INTERESTS

The authors declare no competing interests.

ADDITIONAL INFORMATION

Supplementary information The online version contains supplementary material available at <https://doi.org/10.1038/s41534-022-00541-3>.

Correspondence and requests for materials should be addressed to Mikael Afzelius.

Reprints and permission information is available at <http://www.nature.com/reprints>

Publisher's note Springer Nature remains neutral with regard to jurisdictional claims in published maps and institutional affiliations.



Open Access This article is licensed under a Creative Commons Attribution 4.0 International License, which permits use, sharing, adaptation, distribution and reproduction in any medium or format, as long as you give appropriate credit to the original author(s) and the source, provide a link to the Creative Commons license, and indicate if changes were made. The images or other third party material in this article are included in the article's Creative Commons license, unless indicated otherwise in a credit line to the material. If material is not included in the article's Creative Commons license and your intended use is not permitted by statutory regulation or exceeds the permitted use, you will need to obtain permission directly from the copyright holder. To view a copy of this license, visit <http://creativecommons.org/licenses/by/4.0/>.

© The Author(s) 2022